HTML ABSTRACT * LINKS

JOURNAL OF APPLIED PHYSICS **97**, 103523 (2005)

Stress evolution in GaAsN alloy films

M. Reason, X. Weng, W. Ye, D. Dettling, S. Hanson, G. Obeidi, and R. S. Goldman[a)]
Department of Materials Science and Engineering, University of Michigan, Ann Arbor, Michigan 48109-2136

(Received 9 July 2004; accepted 9 March 2005; published online 11 May 2005)

We have investigated stress evolution in dilute nitride $GaAs_{1-x}N_x$ alloy films grown by plasma-assisted molecular-beam epitaxy. For coherently strained films ($x<2.5\%$), a comparison of stresses measured via *in situ* wafer curvature measurements, with those determined from x-ray rocking curves using a linear interpolation of lattice parameter and elastic constants, suggests significant bowing of the elastic properties of GaAsN. The observed stress differences are used to quantify the composition-dependent elastic constant bowing parameters. For films with $x>2.5\%$, *in situ* wafer curvature measurements reveal a signature for stress relaxation. Atomic force microscopy and transmission electron microscopy measurements indicate that stress relaxation occurs by a combination of elastic relaxation via island formation and plastic relaxation associated with the formation of stacking faults. © *2005 American Institute of Physics*. [DOI: 10.1063/1.1900289]

I. INTRODUCTION

For many group III-V-N alloys, significant energy-band-gap bowing has been predicted and observed.[1–7] For example, for $\sim 1\%$ N added to GaAs, the band gap is reduced by ~ 200 meV.[4–7] The resulting narrow gap nitride semiconductors are promising for a wide range of applications, including long-wavelength light emitters and detectors, high-performance electronic devices, and high efficiency solar cells.[2] In the case of GaAs:N, theoretical studies have predicted that the structural[8] and optical[9] properties depend on the strain state. To date, few experimental studies of stress relaxation in GaAsN have been reported,[10–12] and stress evolution during the growth of GaAsN has apparently not been reported. High-resolution x-ray diffraction (HRXRD) studies[10–12] have suggested that strain relaxation in GaAsN films begins at thicknesses greater than the critical thickness for misfit dislocation generation, as predicted by the Matthews and Blakeslee mechanical equilibrium model.[13] Since HRXRD studies are typically interpreted using a linear interpolation of lattice and elastic constants (i.e., Vegard's law),[10–12] the stresses determined from HRXRD studies may be of limited accuracy. Evidence for deviation from Vegard's law for the lattice parameter of GaAsN has been observed,[14,15] but the effect of this deviation on quantitative stress measurements using HRXRD has apparently not been considered. Furthermore, recent studies have suggested that either the shear deformation potential or the binary elastic constants of GaAsN have an unusual composition dependence,[16,17] although this has not yet been quantified. In addition, theoretical studies have predicted bowing of the elastic constants in alloys such as GaInSb,[18] CdZnTe,[19] and SiGeC.[20]

In this paper, we present a study of stress evolution during the growth of $GaAs_{1-x}N_x$ alloy films up to $x=3.0\%$, using a combination of *in situ* and *ex situ* measurements. For all films with $x<2.5\%$, we observe negligible stress relaxation both during and after film growth. For films with $x>2.5\%$, we identify an *in situ* signature for stress relaxation. The stress relaxation is attributed to a combination of elastic relaxation via island formation and plastic relaxation associated with the formation of stacking faults. In addition, for the coherently strained films, the stress determined from x-ray rocking curves (XRCs), using a linear interpolation of lattice parameters and elastic constants, is consistently higher than the stress measured *directly* by wafer curvature measurements. These stress differences are significantly greater than the stress induced by differential thermal expansion during the process of quenching the sample from the growth temperature to room temperature. Although independent measurements of N content by XRC and nuclear reaction analysis reveal deviation from Vegard's law for the GaAsN lattice parameter, these deviations cannot account for the differences in apparent stress. Instead, these stress differences suggest significant bowing of the elastic properties of GaAsN.

The article is organized as follows. In Sec. II, we describe the methods for synthesizing and characterizing the films, including molecular-beam epitaxy (MBE), multibeam optical stress sensor (MOSS) measurements, XRCs, nuclear reaction analysis (NRA), transmission electron microscopy (TEM), and atomic force microscopy (AFM). Sections III and IV describe investigations of stress evolution for coherently strained films and partially relaxed films, respectively. In Sec. V, various models for alloy lattice parameters are discussed, and evidence for deviation of the GaAsN lattice parameter from Vegard's law is presented. In Sec. VI, evidence for bowing of the elastic properties in coherently strained GaAsN films is presented and discussed. Conclusions are given in Sec. VII.

II. EXPERIMENTAL PROCEDURES

The $GaAs_{1-x}N_x$ alloy films were grown on epiready (001) GaAs by MBE, using solid As_4 and Ga, and a radio frequency (rf) plasma source, with ultrahigh-purity 10%

[a)]Author to whom correspondence should be addressed; electronic mail: rsgold@umich.edu

 © 2005 American Institute of Physics

N_2/Ar. The N composition in the $GaAs_{1-x}N_x$ layers, x, was adjusted by varying the GaAs growth rate between 0.25 and 1.0 $\mu m/h$.[14] The substrate temperature was monitored using an optical pyrometer, calibrated to the (2×4) to (3×1) and (3×1) to (4×2) GaAs surface reconstruction changes at 500 and 595 °C, respectively.[21]

Each sample contained an initial 500-nm GaAs buffer layer grown at 580 °C. Prior to striking the plasma, in order to avoid converting the surface to GaN, the substrate temperature was lowered to 500 °C, and an additional 20-nm layer of GaAs was grown.[22] Finally, $GaAs_{1-x}N_x$ layers with targeted thickness between 100 and 500 nm, and x in the range from 0.5% to 3.0% were grown at 400 °C. Most of the $GaAs_{1-x}N_x$ layers were grown with a high As_4/Ga beam-equivalent pressure (BEP) ratio (>30), except when noted otherwise.

We monitored the film stress in real time, using *in situ* wafer curvature measurements, with a k-Space Associates MOSS system.[23] In this measurement, a laser beam is passed through an étalon in order to produce three parallel output beams. These beams pass through the center viewport of the MBE source flange, and are reflected from the sample into a charged couple device camera. Monitoring fractional changes in the spacing between these reflected spots, $\delta d/d_0$, or the mean differential spacing (MDS), enables a direct measurement of changes in the wafer radius of curvature. The radius of curvature is in turn related to the stress in the film, σ, using Stoney's equation, which assumes that the film thickness is much smaller than the substrate thickness.[24] Using the convention that decreasing beam spacing is negative, and tensile stress is positive, the stress × thickness product, σh_f, is related to the MDS as follows:

$$\sigma h_f = -\left(\frac{\delta d}{d_0}\right)\frac{M_s h_s^2 \cos\alpha}{12L}, \quad (1)$$

where α is the angle of incidence, measured with respect to the sample normal, L is the total optical path length from the sample surface to the detector, M_s is the biaxial modulus of the substrate, and h_s and h_f are the substrate and film thickness, respectively.

In order to minimize external stress on the substrate, the substrates were mounted in In-free sample holders which allow them to flex during growth. Full 3-in. substrates were clamped in the substrate holder using a retaining ring which only contacts the perimeter of the wafer. Benchtop MOSS measurements of bare and mounted substrates reveal that the change in curvature due to external stress from the substrate holder is much less than the changes in curvature due to film mismatch stress during the growth of our GaAsN films. For the 600-μm-thick GaAs substrates used in these experiments, the sensitivity is approximately 1.5 GPa nm. Thus, for a 100-nm-thick film, changes in stress as small as 0.015 GPa can be detected by MOSS. Since MOSS stress measurements are performed at a growth temperature of 400 °C, we must consider the stress induced by differential thermal expansion during the process of quenching to room temperature. However, this change in stress is only about 0.002 GPa, which is substantially lower than the average error of the MOSS measurement, typically about 0.02 GPa.

TABLE I. Elastic constants and lattice parameters for GaAs and GaN used for x-ray rocking curve analysis.

	GaAs[a]	GaN[b]
C_{11} (GPa)	119	296
C_{12} (GPa)	53.8	154
a (Å)	5.6533	4.5

[a]Reference 25.
[b]Reference 26.

Following growth, high-resolution x-ray diffraction measurements were performed in a Bede D[1] system. For each film, symmetric (004) and asymmetric (224) rocking curves were collected at several azimuthal angles in order to take into account any nonzero angle of rotation of the epilayer planes about an in-plane axis (epilayer tilt). The intrinsic film lattice parameter, residual stress and strain, strain relaxation, and effective N composition, x, were calculated using a linear interpolation of the binary elastic constants given in Table I,[25,26] and various lattice-parameter models discussed in Sec. V. For comparison, the (004) rocking curves were simulated using RADS.[27] The program is based on the Takagi–Taupin dynamical theory of x-ray diffraction, which uses the two-beam approximation and assumes that only the incident and diffracted waves have appreciable amplitude.[28] Nitrogen concentrations were also determined using NRA with the $^{14}N(d,\alpha_1)^{12}C$ reaction. Details of the NRA experiment are discussed elsewhere.[29]

For TEM studies, cross-sectional specimens were prepared using conventional mechanical thinning followed by argon-ion milling at 77 K. Diffraction-contrast TEM imaging and high-resolution TEM (HRTEM) were carried out in a JEOL 2010FX transmission electron microscope operating at 200 keV. We also examined the surface morphology of the films with tapping mode AFM, using a Digital Instruments Nanoscope IIIa.

III. COHERENTLY STRAINED GaAsN FILMS

Figures 1(a)–1(c) show representative AFM images for 100-nm-thick coherently strained GaAsN films grown with As_4/Ga ratios of (a) 7, (b) 18, and (c) 30. For films with a high As_4/Ga ratio, surface features elongated along the $[1\bar{1}0]$ direction are observed, and the rms roughness is 0.4±0.1 nm. For films grown with an intermediate As_4/Ga ratio, the rms roughness is slightly higher, 0.8±0.1 nm, and the density of features elongated along the $[1\bar{1}0]$ direction is much lower. Finally, for films grown with a low As_4/Ga ratio, the rms roughness increases to approximately 16 nm, and dome-shaped features are evident. Since As_4/Ga ratios of 30 were found to lead to the smoothest film surface, all films were grown with an As_4/Ga ratio of ~30 unless otherwise noted.

Figure 2(a) shows MOSS measurements of the stress × thickness product, σh_f, as a function of film thickness, h_f, during the growth of 500-nm-thick $GaAs_{1-x}N_x$ layers with various x. For all samples with $x \leqslant 2.5\%$, the slope of σh_f vs h_f is proportional to the nitrogen composition deter-

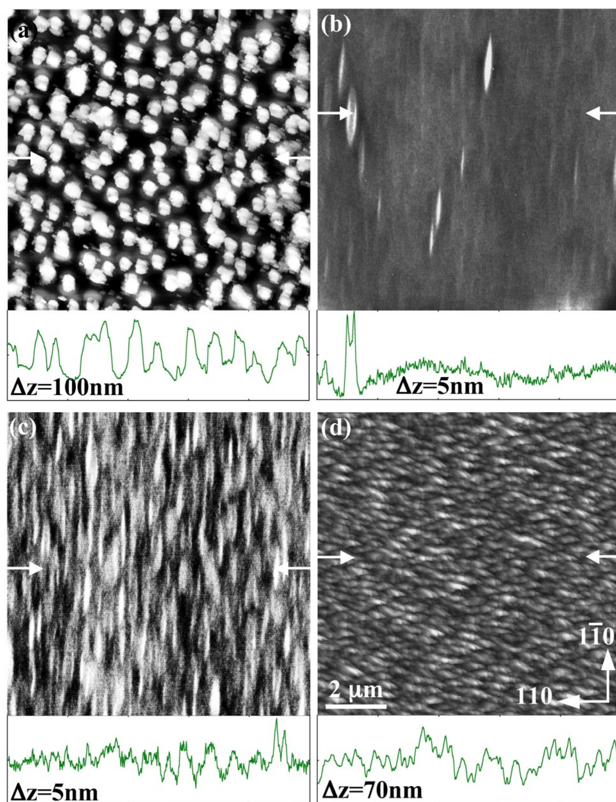

FIG. 1. (Color online) Atomic force microscopy (AFM) images of the surfaces of 100-nm-thick, coherently strained GaAsN films grown with As_4/Ga=(a) 7, (b) 18, and (c) 29. A 250-nm-thick, partially-relaxed GaAsN film is shown in (d). The gray-scale ranges displayed are (a) 100, (b) 5, (c) 5, and (d) 70 nm. Cuts of the tip height defined by the arrows are shown below each AFM image.

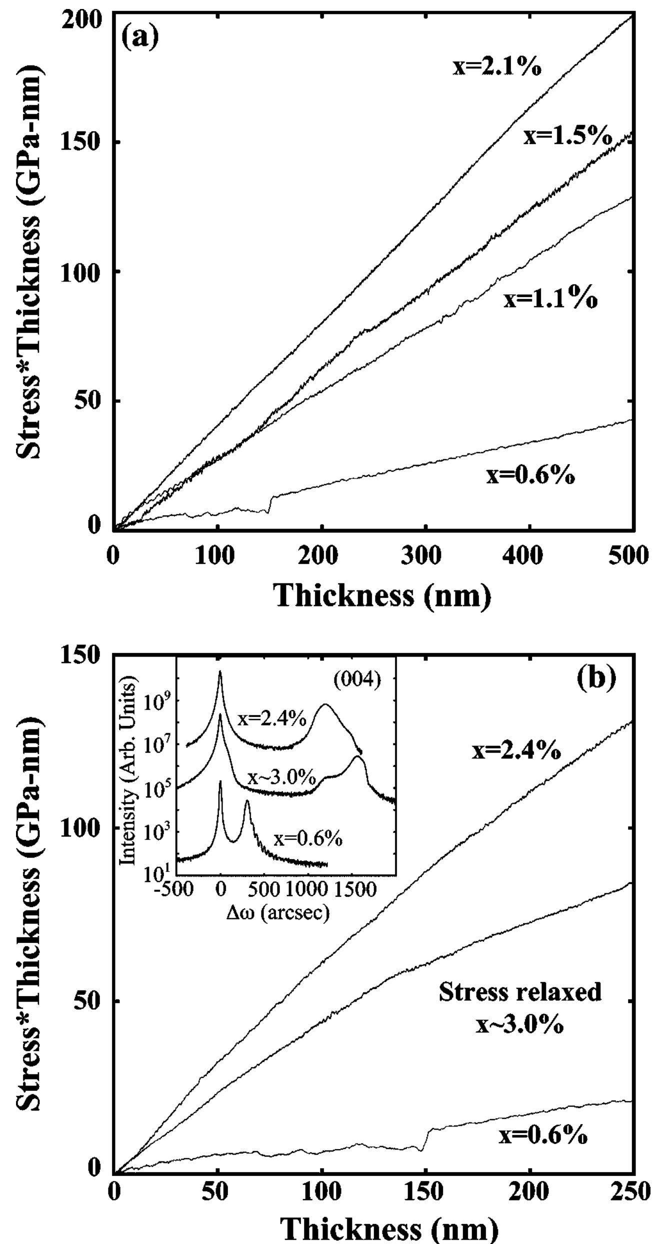

FIG. 2. Stress-thickness product vs thickness for (a) 500-nm-thick $GaAs_{1-x}N_x$ films and (b) the first 250 nm of $GaAs_{1-x}N_x$ films. In (a), the slope is approximately constant for all films, indicating negligible stress relaxation. In (b), the slope is approximately constant for films with $x < 2.5\%$, while for $x \geq 2.5\%$ the slope begins to decrease, indicating stress relaxation. Inset: (004) XRC for the same films. For $x < 2.5\%$, there is one distinct epilayer peak, while for $x \geq 2.5\%$ there is a split epilayer peak.

mined from XRC. In addition, the slope of σh_f vs h_f remains approximately constant throughout the film growth, indicating negligible stress relaxation. This is in agreement with *ex situ* XRC measurements, which also confirmed that all films were coherently strained.

A comparison of the stresses determined using MOSS measurements of wafer curvature with those determined from XRC using a linear interpolation of lattice and elastic constants is shown in Fig. 3(a). For the $GaAs_{1-x}N_x$ films with $x < 1.3\%$, MOSS and XRC stresses are similar except when the As_4/Ga BEP ratio is low. The apparent MOSS and XRC stress differences for films with low As_4/Ga BEP ratios are likely related to the observed increase in surface roughness in those films, shown in Figs. 1(a) and 1(b). The increase in surface roughness would likely lead to a decrease in the surface stress, which would in turn lower the apparent stress measured by MOSS.[30–32] For XRC measurements, surface roughness would result in the broadening of the epilayer peak, but would not likely influence calculations of the film stress.[33]

For the $GaAs_{1-x}N_x$ films with $As_4/Ga \sim 30$, XRC stresses tend to be higher than the MOSS stresses, even though their surfaces were relatively smooth. Furthermore, the differences between XRC and MOSS stresses increase as the N composition increases. For films with $x > 1.3\%$, the differences between the XRC and MOSS stresses are larger than the error bars, and significantly greater than the stress induced by differential thermal expansion during the process of quenching the sample from the growth temperature to room temperature, which is ~0.002 GPa. MOSS provides a direct measurement of film stress. However, the XRC stresses are based upon several assumptions including a linear interpolation of GaAs and GaN lattice parameter and elastic constants. Therefore, a significant bowing of the lattice parameter or elastic constants of GaAsN alloys is likely determining the apparent differences in MOSS and XRC stresses. Bowing of the lattice parameter and elastic constants will be discussed in Secs. V and VI, respectively.

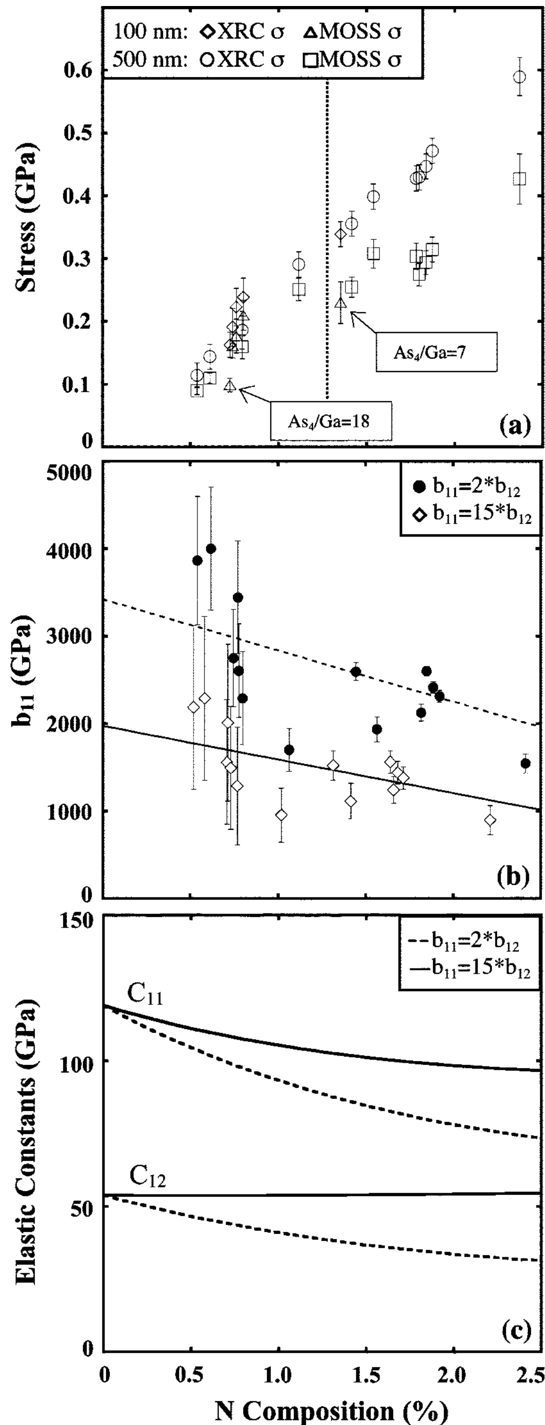

FIG. 3. (a) Stress measured by *in situ* multibeam optical stress sensor (MOSS) (triangles and squares) measurements and calculated from *ex situ* x-ray rocking curve (XRC) (diamonds and circles) measurements using a linear interpolation of lattice parameter and elastic constants. For samples with N composition greater than ~1.3%, indicated by the dotted line, the apparent stress difference is significantly greater than the error bars of the measurements. All samples were grown with a high As_4/Ga ratio (⩾30), unless otherwise noted. N compositions were determined from XRCs using a linear interpolation of lattice parameters and elastic constants. (b) Composition dependence of the bowing parameter, b_{11}, for which the MOSS and XRC stresses are equal, shown as open diamonds and solid circles for b_{11}/b_{12}=2 and 15, respectively. Weighted linear fits to the data points for b_{11}/b_{12}=2 and 15 are indicated by the dashed and solid lines, respectively. N compositions were determined from XRCs, with bowing of the elastic constants included. (c) Composition dependence of C_{11} and C_{12} using b_{ij} for which the MOSS and XRC stresses are equal, with b_{11}/b_{12}=15 (solid lines) and b_{11}/b_{12}=2 (dashed lines).

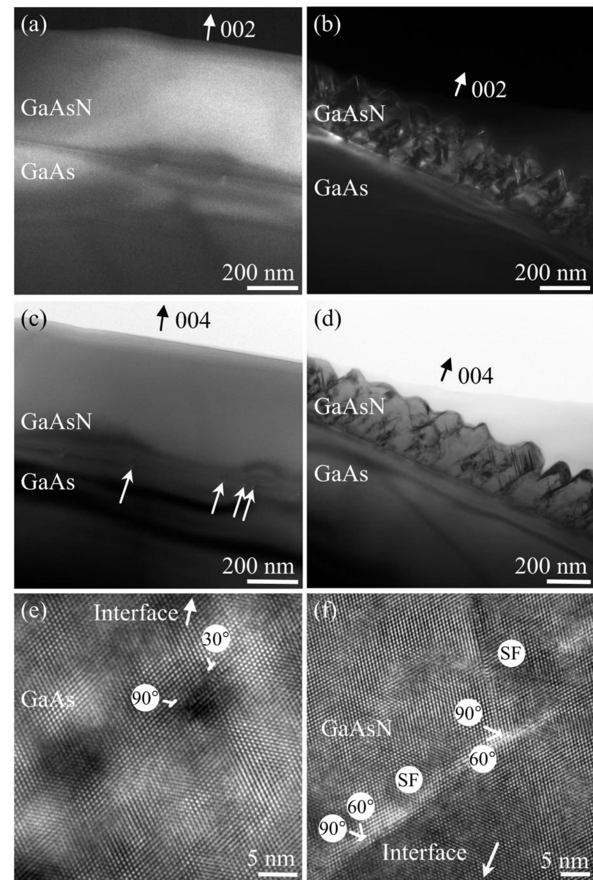

FIG. 4. Dark-field cross-sectional transmission electron microscopy (TEM) images for $GaAs_{1-x}N_x$ films with x=(a) 2.4% and (b) 3.0%, collected with a [002] two-beam condition. In addition, bright-field cross-sectional TEM images collected with a [004] two-beam condition are shown for x=(c) 2.4% and (d) 3.0%. Finally, cross-sectional high-resolution TEM images are shown for x=(e) 2.4% and (f) 3.0%. In both cases, the zone axis is ⟨110⟩.

IV. STRESS RELAXATION IN GaAsN FILMS

In Fig. 2(b), we present MOSS measurements of σh_f vs h_f during the first 250 nm of growth of $GaAs_{1-x}N_x$ layers with x=0.6%, 3.0%, and 2.4%; (004) XRCs for these films are shown in the inset. For films with $x<2.5\%$, the slope of σh_f vs h_f remains approximately constant throughout the growth, indicating that negligible stress relaxation has occurred. Meanwhile, AFM reveals a fairly smooth surface, with features and rms roughness essentially identical to those shown in Fig. 1(c). In addition, XRC reveals one distinct epilayer peak, suggesting homogeneous incorporation of nitrogen throughout the GaAsN film. However, for films with $x \geqslant 2.5\%$, the slope of σh_f vs h_f is initially constant, then decreases at a film thickness of ~140 nm, suggesting the onset of stress relaxation. AFM reveals a rms roughness of approximately 20 nm, as shown in Fig. 1(d). The increase in surface roughness for films with $x>2.5\%$ suggests the initiation of elastic relaxation of stress via island formation. In addition, XRC reveals a split epilayer peak. According to dynamical x-ray diffraction simulations, this split epilayer peak may be accounted for by a vertical gradient in either composition or strain relaxation.

To investigate the possible occurrence of alloy phase separation or plastic strain relaxation in films with $x>2.5\%$,

we performed a variety of cross-sectional TEM measurements. In Figs. 4(a) and 4(b), we present large-scale dark-field cross-sectional TEM images, collected with a [002] two-beam condition, for $GaAs_{1-x}N_x$ films with (a) $x=2.4\%$ and (b) $x=3.0\%$. In earlier studies, alloy phase separation within $GaAs_{1-x}N_x$ films was apparently revealed by the presence of lateral contrast variations in [002] dark-field TEM images.[10] However, similar contrast is not observed in Figs. 4(a) and 4(b), suggesting that alloy phase separation has not occurred in our case. Figures 4(c) and 4(d) show large-scale bright-field cross-sectional TEM images of $GaAs_{1-x}N_x$ films with (c) $x=2.4\%$ and (d) $x=3.0\%$, collected with a [004] two-beam condition. For the $x=2.4\%$ $GaAs_{1-x}N_x$ film, shown in Fig. 4(c), dislocations are observed at the epilayer/substrate interface, as indicated by the white arrows. Meanwhile, the GaAsN film is apparently free of dislocations. However, for the $x=3.0\%$ film, shown in Fig. 4(d), a high density of stacking faults is observed within the GaAsN film, consistent with other literature reports of GaAsN with high N composition.[10,34]

We quantified misfit components associated with the dislocations and stacking faults in Figs. 4(c) and 4(d) using HRTEM. High-resolution views of the $GaAs_{0.976}N_{0.024}/GaAs$ interface, such as Fig. 4(e), reveal a dissociated 60° dislocation. The 30° partial lies near the interface, while the 90° partial lies within the GaAs substrate, typical of epitaxial films grown under tension.[35,36] The 90° partial has a misfit (edge) component of $a/3\sqrt{2}$, where a is the unstrained epilayer lattice constant, while the 30° partial has no misfit component.[36] The linear density of dislocations at the film/substrate interface was 3.9 μm^{-1}, corresponding to an estimated strain relaxation of less than 10%, consistent with MOSS and XRC values of ~5%. Figure 4(f) presents a high-resolution image of two stacking faults within the $GaAs_{0.974}N_{0.026}$ film. In this case, each stacking fault is bound by a 90° partial and 60° dislocation.[35] It is likely that 90° partials nucleate at the surface during island formation and glide towards the interface. In the case of parallel misfit components of a 90° partial and a 60° dislocation, repulsive stress fields restrict the glide of the 90° partial, leading to the formation of a stacking fault.[35] The net misfit component is $a/6\sqrt{2}$ and the linear density of stacking faults in the $GaAs_{0.976}N_{0.024}$ film is 82 μm^{-1}. In this case, the misfit strain is significantly relaxed. Therefore, the decrease in MOSS stress for the $x=3.0\%$ film in Fig. 2(b) is likely due to both elastic relaxation via island formation and plastic relaxation associated with the formation of stacking faults.

V. DEVIATION OF LATTICE PARAMETER FROM VEGARD'S LAW

The lattice parameter of a ternary GaAsN alloy film, $a_{GaAs_{1-x}N_x}$, is typically assumed to follow a linear interpolation of the binary lattice parameters (i.e., Vegard's law),[37]

$$a_{GaAs_{1-x}N_x} = x a_{GaN} + (1-x) a_{GaAs}. \tag{2}$$

However, evidence for deviation from Vegard's law has been observed for GaAsN,[14,15] and this deviation may cause the stresses determined from HRXRD studies to be of limited

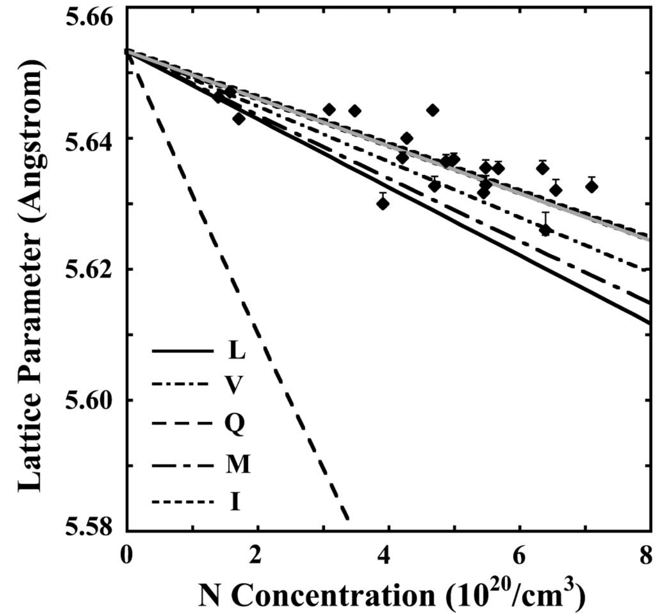

FIG. 5. GaAsN alloy lattice parameter vs nitrogen concentration, predicted by various lattice-parameter models, as well as observed experimentally by x-ray rocking curves (y axis) and nuclear reaction analysis (Ref. 29) (x axis). The L model assumes a linear interpolation of the binary lattice parameters (i.e., Vegard's law), the V model assumes a linear interpolation of the binary unit-cell volumes, the Q model assumes a quadratic interpolation of the binary unit-cell volumes, the M model uses Murnaghan's equation of state to minimize the strain energy, and in the I model, the linearly interpolated lattice parameter is modified to include the effect of lattice expansion due to the incorporation of N–N split interstitials. The gray line indicates the least-squares fit to the experimental data.

accuracy. As discussed in Sec. III, we have observed significant differences between the stresses measured directly by MOSS and calculated from XRC measurements assuming Vegard's law.

There are several other possible models which relate the lattice parameter of a ternary alloy to those of its binary constituents. In addition to interpolation of lattice parameters (i.e., Vegard's law), we considered four different models for the composition dependence of $a_{GaAs_{1-x}N_x}$, referred to as V, Q, M, and I. The V model assumes a linear interpolation of the binary unit-cell volumes,

$$(a_{GaAs_{1-x}N_x})^3 = x V_{GaN} + (1-x) V_{GaAs}. \tag{3}$$

The second model, Q, assumes a quadratic interpolation of the binary unit-cell volumes,

$$(a_{GaAs_{1-x}N_x})^3 = \frac{[x B_{GaN} + (1-x) B_{GaAs}] V_{GaN} V_{GaAs}}{x B_{GaN} V_{GaN} + (1-x) B_{GaAs} V_{GaAs}}, \tag{4}$$

where B is the bulk modulus. In the third model, M,

$$(a_{GaAs_{1-x}N_x})^3 = V_M, \tag{5}$$

where V_M is the volume which minimizes the strain energy, F, in Murnaghan's equation of state,

$$F = \frac{B_{GaAs}}{B'_{GaAs}} \left(\frac{V_{GaAs}}{V_M} \right)^{B'_{GaAs}} + \frac{B_{GaN}}{B'_{GaN}} \left(\frac{V_{GaN}}{V_M} \right)^{B'_{GaN}}, \tag{6}$$

where B' is the derivative of the bulk modulus with respect to pressure at the equilibrium volume.[38] Finally, in the I

TABLE II. Stress measured by multibeam optical stress sensor (MOSS) and determined from x-ray rocking curve (XRC) measurements assuming different models for the film lattice parameter, for six samples with various N compositions. The *L* model assumes a linear interpolation of the binary lattice parameters (i.e., Vegard's law). The *I* model accounts for deviation from a linear interpolation due to lattice expansion caused by the incorporation of N–N split interstitials.

N comp. (%)	MOSS σ (±0.02 GPa)	XRC σ *L* Model (±0.015 GPa)	XRC σ_I *I* Model (±0.015 GPa)
1.42	0.26	0.356	0.358
1.54	0.31	0.399	0.402
1.78	0.30	0.428	0.431
1.79	0.28	0.430	0.434
1.84	0.29	0.447	0.450
1.87	0.32	0.472	0.476

model, the linearly interpolated lattice parameter is modified to include the effect of lattice expansion from the incorporation of N–N split interstitials,[39]

$$a_{\mathrm{GaAs}_{1-x}\mathrm{N}_x} = a_{\mathrm{GaAs}}\left\{1 + \frac{C_{11}+2C_{12}}{C_{11}}\frac{x}{2}\left[f\frac{r_{\mathrm{N}}-r_{\mathrm{As}}}{r_{\mathrm{Ga}}+r_{\mathrm{As}}} + (1-f)\frac{d_b - r_{\mathrm{Ga}} - r_{\mathrm{As}}}{r_{\mathrm{Ga}}+r_{\mathrm{As}}}\right]\right\}, \tag{7}$$

where $f \sim 0.8$ is the fraction of nitrogen which incorporates substitutionally, which we measured by NRA,[29] r_{N}, r_{As}, and r_{Ga} are the covalent radii of N, As, and Ga, respectively, and

$$d_b = \frac{\sqrt{3}}{3} r_{\mathrm{N}} + \sqrt{(r_{\mathrm{N}}+r_{\mathrm{As}})^2 - \tfrac{2}{3} r_{\mathrm{N}}^2}. \tag{8}$$

Figure 5 presents the $\mathrm{GaAs}_{1-x}\mathrm{N}_x$ alloy lattice parameter predicted by the L, V, Q, M, and I models, and experimentally observed by XRC vs N concentration measured by NRA.[29] The data points for XRC lattice parameter were determined assuming a linear interpolation of the GaAsN elastic constants, while the error bars take into account bowing of the elastic constants (to be discussed in Sec. VI). The Q (V, M, and I) model predicts smaller (larger) lattice parameters than those predicted using Vegard's law. Meanwhile, the independent XRC and NRA measurements suggest a lattice parameter larger than predicted by Vegard's law. A linear least-squares fit to the XRC and NRA data indicates that the deviation from Vegard's law is most accurately predicted by the I model.

Table II presents the *in situ* stress measured using MOSS, along with the residual stress calculated from XRC measurements using a linear interpolation of lattice parameters, as well as the I lattice-parameter model. However, the stress calculated when assuming the I model is only slightly different than the stress determined assuming a linear interpolation of lattice parameters. Therefore, the difference between the measured MOSS σ and calculated XRC σ cannot be explained using the models for lattice parameter. Instead, bowing of the elastic constants is likely determining the differences in MOSS and XRC stresses, as discussed in Sec. VI.

VI. BOWING OF GaAsN ELASTIC CONSTANTS

The elastic constants of $\mathrm{GaAs}_{1-x}\mathrm{N}_x$ alloys, $C_{ij}(\mathrm{GaAs}_{1-x}\mathrm{N}_x)$, are defined as follows:

$$C_{ij}(\mathrm{GaAs}_{1-x}\mathrm{N}_x) = x\, C_{ij}(\mathrm{GaN}) + (1-x)C_{ij}(\mathrm{GaAs}) - b_{ij}\, x(1-x), \tag{9}$$

where a linear interpolation of binary elastic constants occurs if $b_{ij}=0$, and nonzero values of b_{ij} imply deviation from the linear interpolation, so-called "bowing" of the elastic properties. In order to quantify b_{ij} for GaAsN alloys, we determined the composition dependence of b_{ij} for which the MOSS and XRC stresses are equal. Since we have one equation (MOSS σ=XRC σ), and two unknowns (b_{11} and b_{12}), we must make an assumption for the b_{11}/b_{12} ratio. Theoretical studies have predicted $b_{11}/b_{12}=2$ and 4 for the alloys $\mathrm{Ga}_x\mathrm{In}_{1-x}\mathrm{Sb}$ (Ref. 18) and $\mathrm{Cd}_{1-x}\mathrm{Zn}_x\mathrm{Te}$,[19] respectively. In addition, $b_{11}/b_{12}=3.5$, 12, and 16 have been predicted for $\mathrm{Si}_{0.59}\mathrm{Ge}_{0.396}\mathrm{C}_{0.014}$, $\mathrm{Si}_{0.813}\mathrm{Ge}_{0.123}\mathrm{C}_{0.064}$, and $\mathrm{Si}_{0.734}\mathrm{Ge}_{0.232}\mathrm{C}_{0.033}$, respectively.[20] Since GaInSb is a III-V compound, we have considered a ratio of $b_{11}/b_{12}=2$ for GaAsN. Although SiGeC is not a III-V compound, the small size and low concentration of carbon atoms in SiGe are similar to those of nitrogen atoms in GaAs. In addition, significant interstitial incorporation has been observed for both C in SiGeC (Refs. 40 and 41) and N in GaAsN.[14,29] Since $\mathrm{Si}_{0.734}\mathrm{Ge}_{0.232}\mathrm{C}_{0.033}$ grown on Si has a similar lattice mismatch to that of our GaAsN films on GaAs, we have also considered a similar b_{11}/b_{12} ratio of 15.

In Fig. 3(b), the bowing parameters, b_{11}, are plotted versus N composition, for $b_{11}/b_{12}=2$ and 15, shown as solid circles and open diamonds, respectively. Weighted linear fits to the data points are indicated by the dashed and solid lines, for $b_{11}/b_{12}=2$ and 15, respectively. As b_{11}/b_{12} increases, the b_{11} bowing parameter decreases. In addition, as the N composition increases, the differences between the MOSS and XRC stresses become more significant than the stress measurement error bars. Although the elastic constant bowing parameters, b_{ij}, for GaAsN are significantly larger than those predicted for GaInSb (Ref. 18) and SiGeC,[20] similarly larger band-gap energy bowing parameters have also been reported for GaAsN (44 eV) (Refs. 42 and 43) in comparison with those of GaInSb (0.4 eV) (Ref. 44) and AlGaAs (0.2 eV).[44,45] We also observe that b_{ij} is composition dependent, decreasing with increasing N composition, similar to the trends reported for the band-gap energy bowing parameter for GaAsN.[42,43] For many ternary compound semiconductor alloys, bowing of the physical properties is often attributed to lattice disorder.[18,46,47] Thus, similar trends for bowing of both the elastic constants and band-gap energies are expected.

Using the bowing parameters in Fig. 3(b), we determined the resulting elastic constants, C_{11} and C_{12}. Figure 3(c) presents a plot of C_{11} and C_{12} vs N composition, shown as the dashed and solid lines for $b_{11}/b_{12}=2$ and 15, respectively. The difference in the elastic constants using b_{11}/b_{12} =2 and 15 increases with N composition, with ~25% difference for $x=2.5\%$. The bowing of the elastic constants is presumably due to the small size of nitrogen. Lattice relaxation around nitrogen impurities creates shear strain, which

splits the valence band around the impurity site. It has been predicted that this valence-band splitting causes bowing of either the shear deformation potential or the elastic constants.[16]

VII. CONCLUSIONS

In summary, we have investigated stress evolution in $GaAs_{1-x}N_x$ films using a combination of *in situ* MOSS, in comparison with *ex situ* XRC, AFM, and TEM. For films with $x < 2.5\%$, the film stress is proportional to x, and remains approximately constant during growth, indicating that the films are coherently strained. On the other hand, for films with $x > 2.5\%$, stress relaxation is observed during growth. This relaxation is apparently due to a combination of elastic relaxation via island formation and plastic relaxation associated with the formation of stacking faults. In addition, the stresses determined by XRC for coherently strained films are consistently higher than those measured using MOSS, with the apparent stress differences increasing significantly as the N composition increases. The differences between the MOSS and XRC stresses cannot be explained by the stress induced by differential thermal expansion during the process of quenching from the growth temperature to room temperature, or by the deviation of the GaAsN lattice parameter from Vegard's law. The differences instead reveal significant bowing of the GaAsN elastic constants.

ACKNOWLEDGMENTS

This work was supported in part by the National Science Foundation Early Faculty CAREER, Instrumentation for Materials Research, and Nanoscale Exploratory Research Programs (Grant Nos. 9773707, 9975701, and 0210714); the DoD Multidisciplinary University Research Initiative administered by the Air Force Office of Scientific Research under Grant No. F49620-00-1-0328; the Department of Energy, through the National Renewable Energy Laboratory Photovoltaics Beyond the Horizon Program under Contract No. ACQ-1-30619-14; the TRW Foundation; and k-Space Associates, Inc. The authors thank S.-H. Wei, P. Carrier, and M. D. Thouless for useful discussions and acknowledge the assistance of the staff of the Electron Microbeam Analysis Laboratory (EMAL) at the University of Michigan. The JEOL 2010 FX analytical electron microscope at EMAL is supported by NSF under Grant No. 9871177.

[1] M. Weyers, M. Sato, and H. Ando, Jpn. J. Appl. Phys., Part 2 **31**, L853 (1992).
[2] I. A. Buyanova, W. M. Chen, and B. Monemar, MRS Internet J. Nitride Semicond. Res. **6**, 2 (2001).
[3] L. Bellaiche, S.-H. Wei, and A. Zunger, Phys. Rev. B **54**, 17568 (1996).
[4] W. G. Bi and C. W. Tu, Appl. Phys. Lett. **70**, 1608 (1997).
[5] J. Salzman and H. Temkin, Mater. Sci. Eng., B **50**, 148 (1997).
[6] A. Nishikawa, R. Katayama, K. Onabe, and Y. Shiraki, J. Cryst. Growth **251**, 427 (2003).
[7] K. Uesugi, N. Morooka, and I. Suemune, Appl. Phys. Lett. **74**, 1254 (1999).
[8] D. Schlenker *et al.*, Jpn. J. Appl. Phys., Part 1 **39**, 5751 (2000).
[9] L. Bellaiche, S.-H. Wei, and A. Zunger, Appl. Phys. Lett. **70**, 3558 (1997).
[10] I. Suemune, K. Uesugi, and T.-Y. Seong, Semicond. Sci. Technol. **17**, 755 (2002).
[11] W. K. Cheah, W. J. Fan, S. F. Yoon, S. Z. Wang, and W. K. Loke, J. Appl. Phys. **94**, 3828 (2003).
[12] J. Toivonen *et al.*, J. Mater. Sci.: Mater. Electron. **14**, 267 (2003).
[13] J. W. Matthews and A. E. Blakeslee, J. Cryst. Growth **27**, 118 (1974).
[14] S. G. Spruytte, M. C. Larson, W. Wampler, C. W. Coldren, H. E. Petersen, and J. S. Harris, J. Cryst. Growth **227**, 506 (2001).
[15] W. J. Fan, S. F. Yoon, T. K. Ng, S. Z. Wang, W. K. Loke, R. Liu, and A. Wee, Appl. Phys. Lett. **80**, 4136 (2002).
[16] Y. Zhang, A. Mascarenhas, H. P. Xin, and C. W. Tu, Phys. Rev. B **61**, 4433 (2000).
[17] M. H. Ya, Y. F. Chen, and Y. S. Huang, J. Appl. Phys. **92**, 1446 (2002).
[18] N. Bouarissa, Mater. Sci. Eng., B **100**, 280 (2003).
[19] A. E. Merad, H. Aourag, B. Khelifa, C. Mathieu, and G. Merad, Superlattices Microstruct. **30**, 241 (2001).
[20] P. C. Kelires, Appl. Surf. Sci. **102**, 12 (1996).
[21] H. Shtrikman (private communication).
[22] D. W. Gotthold, S. Govindaraju, T. Mattord, A. L. Holmes, and B. G. Streetman, J. Vac. Sci. Technol. A **18**, 461 (2000).
[23] J. A. Floro, E. Chason, S. R. Lee, R. D. Twesten, R. Q. Hwang, and L. B. Freund, J. Electron. Mater. **26**, 969 (1997).
[24] G. G. Stoney, Proc. R. Soc. London, Ser. A **82**, 172 (1909).
[25] K. Kim, W. R. L. Lambrecht, and B. Segall, Phys. Rev. B **53**, 16310 (1996).
[26] O. Madelung, *Semiconductors-Basic Data*, 2nd rev. ed. (Springer, Berlin, 1996), p. 105.
[27] *Rocking Curve Analysis by Dynamical Simulation*, Bede Scientific, Inc.
[28] M. Wormington, C. Panaccione, K. M. Matney, and D. K. Bowen, Philos. Trans. R. Soc. London, Ser. A **357**, 2827 (1999).
[29] M. Reason, H. A. McKay, W. Ye, S. Hanson, R. S. Goldman, and V. Rotberg, Appl. Phys. Lett. **85**, 1692 (2004).
[30] R. E. Martinez, W. M. Augustyniak, and J. A. Golovchenko, Phys. Rev. Lett. **64**, 1035 (1990).
[31] A. J. Schell-Sorokin and R. M. Tromp, Phys. Rev. Lett. **64**, 1039 (1990).
[32] J. P. Silveira and F. Briones, J. Cryst. Growth **202**, 113 (1999).
[33] D. K. Bowen and B. K. Tanner, *High Resolution X-ray Diffractometry and Topography* (Taylor & Francis, London, 1998), pp. 50–60.
[34] S. Thomas, S. White, P. R. Chalker, T. J. Bullough, and T. B. Joyce, J. Mater. Sci.: Mater. Electron. **13**, 525 (2002).
[35] G. Wagner, Cryst. Res. Technol. **33**, 383 (1998).
[36] B. C. De Cooman and C. B. Carter, Acta Metall. **37**, 2765 (1989).
[37] L. Vegard, Z. Phys. **5**, 17 (1921).
[38] L. G. Ferreira, S.-H. Wei, and A. Zunger, Phys. Rev. B **40**, 3197 (1989).
[39] N. F. Chen, Y. Wang, H. He, and L. Lin, Phys. Rev. B **54**, 8516 (1996).
[40] C. Calmes, D. Bouchier, C. Clerc, and Y. Zheng, Appl. Surf. Sci. **224**, 122 (2004).
[41] H. J. Osten, Thin Solid Films **367**, 101 (2000).
[42] U. Tisch, E. Finkman, and J. Salzman, Phys. Status Solidi A **195**, 528 (2003).
[43] A. Khan, N. Nelson, J. A. Griffin, D. J. Smith, T. Steiner, and S. N. Mohammad, Solid-State Electron. **48**, 291 (2004).
[44] M. Ferhat, Phys. Status Solidi B **241**, R38 (2004).
[45] L. H. Robins, J. T. Armstrong, R. B. Marinenko, A. J. Paul, J. G. Pellegrino, and K. A. Bertness, J. Appl. Phys. **93**, 3747 (2003).
[46] N. Bouarissa and H. Aourag, Phys. Status Solidi B **199**, 403 (1997).
[47] P. R. C. Kent, L. Bellaiche, and A. Zunger, Semicond. Sci. Technol. **17**, 851 (2002).